Atmospheric
Chemistry
and Physics
Discussions

Chemical characterization and sources of submicron aerosols in the northeastern Qinghai-Tibet Plateau: insights from high-resolution mass spectrometry

Xinghua Zhang[1,2,3], Jianzhong Xu[1], Shichang Kang[1], Qi Zhang[4]

[1]State Key Laboratory of Cryospheric Sciences, Northwest Institute of Eco-Environment and Resources, Chinese Academy of Sciences, Lanzhou 730000, China

[2]Key Laboratory of Arid Climatic Change and Reducing Disaster of Gansu Province, Key Laboratory of Arid Climatic Change and Disaster Reduction of CMA, Institute of Arid Meteorology, China Meteorological Administration, Lanzhou 730020, China

[3]University of Chinese Academy of Sciences, Beijing 100049, China

[4]Department of Environmental Toxicology, University of California, Davis, CA 95616, USA

Correspondence to: Jianzhong Xu (jzxu@lzb.ac.cn)

Abstract

An Aerodyne high-resolution time-of-flight aerosol mass spectrometer (HR-ToF-AMS) was deployed along with other online instruments to study the highly time-resolved chemistry and sources of submicron aerosols (PM_1) at Waliguan (WLG) Baseline Observatory, a high-altitude (3816 m a.s.l.) background station located at the northeastern edge of Qinghai-Tibet Plateau (QTP), during 1−31 July 2017. The average PM_1 mass concentration during this study was 9.1 µg m^{-3} (ranging from 0.3 to 28.1 µg m^{-3}), which was distinct higher than those (2.0–5.7 µg m^{-3}) measured with Aerodyne AMS at other high-elevation sites in the southern or central QTP. Sulfate showed dominant contribution (38.1%) to PM_1 at WLG following by organics (34.5%), ammonium (15.2%), nitrate (8.1%), BC (3.0%) and chloride (1.1%). Accordingly, bulk aerosols appeared to be slightly acidic throughout this study mainly related to the enhanced sulfate contribution. All chemical species peaked at the accumulation mode, indicating the well mixed and highly aged aerosol particles at WLG from long-range transport. Positive matrix factorization (PMF) on the high-resolution organic mass spectra resolved four distinct organic aerosol (OA) components, including a traffic-related hydrocarbon-like OA (HOA), a relatively fresh biomass burning OA (BBOA), an aged biomass burning OA (agBBOA) and a more-oxidized oxygenated OA (OOA). On average, the two relatively oxidized OAs, OOA and agBBOA, contributed 34.4% and 40.4% of organics, respectively, while the rest were 18.4% for BBOA and 6.8% for HOA. Source analysis for air masses displayed higher mass concentrations of PM_1 and enhanced contributions of sulfate and biomass burning related OA components (agBBOA + BBOA) were from northeast of the WLG with shorter transport distance, whereas lower PM_1 mass concentrations with enhanced OOA contribution were from west after long-range transport, suggesting their distinct aerosol sources and significant impacts of regional transport to aerosol mass loadings and chemistry at WLG.

Atmospheric
Chemistry
and Physics
Discussions

1 Introduction

The Qinghai-Tibet Plateau (QTP) is one of the most remote and pristine region in the world. Its huge surface area (~ 2,500,000 km^2) and high elevation (with a mean elevation of more than 4000 m above sea level (a.s.l.)) make it especially important in earth sciences and therefore called as the "third pole" (Yao et al., 2012). According to its high elevation, sparse population and minor local anthropogenic activities, the QTP is regarded as an ideal area for observing the natural background aerosol and long-range transport aerosol. In recent decades, a certain number of studies have presented convincing evidence for the long-range transport of air pollutants from the surrounding areas to the QTP (Engling et al., 2011; Xia et al., 2011; Lüthi et al., 2015; Zhang et al., 2017). Particularly, air pollutants from the southern and southeastern Asia, two of the major regions with enhanced biomass burning emissions in the world, would stack up in the southern foothills of the Himalayas during the pre-monsoon season, then climb over Himalayas by the topographic lifting and the mountain-valley breeze circulation, and finally move upward to QTP (Lüthi et al., 2015). These long-range transport following by deposition of polluted air masses, especially for the two important light-absorbing substances of black carbon (BC) and brown carbon (BrC), have significant impacts on climate, environment and hydrology in the QTP (Xu et al., 2009; Kang et al., 2010; Qian et al., 2011; Yang et al., 2014).

In contrast, aerosol particles in the northern QTP showed quite different behaviors comparing with that in the southern QTP due to the different aerosol sources and climate for these two regions. For example, Li et al. (2016) found equal important contributions from fossil fuel (46%) and biomass (54%) aerosol sources to BC in the Himalayas, however, it was dominated by fossil fuel combustion (66%) in the northern QTP. Correspondingly, the chemical composition of ambient aerosol in the northern QTP was also distinct different with that in the southern QTP. Xu et al. (2014a, 2015) conducted aerosol compositions from filter measurements of PM$_{2.5}$ (particulate matter with diameter less than 2.5 μm) at the Qilian Shan Station observatory at the northeast edge of QTP, and found sulfate was a dominant component during summer season due to the influence of anthropogenic emissions from inland of northwest China. Similar results were also found in Li et al. (2013) and Zhang et al. (2014) which conducted field studies in the northeastern part of QTP. Nitrate, oxidized from NO$_x$, was also an important component in the northern QTP which could interact with mineral dust during transport (Xu et al., 2014a). Due to the relatively lower elevation comparing with the southern QTP (< 4000 vs. > 5000 m a.s.l.), the polluted air masses are easily transported to the mountain areas in the northern QTP forced by the strongly mountain-valley breeze during summer (Xu et al., 2013). In addition, air pollutants to the northern QTP could also from the central Eurasian continent where locates in the upstream of the northwest of China, although relatively lower air masses presented comparing with those impacted by anthropogenic emissions from China and the Indian subcontinent (Xue et al., 2013). However, most of the previous studies in the northeastern QTP for characterizing the chemical properties and sources of aerosol particles were heavily based on the filter or snow/ice samples with low time resolution ranging from days to weeks, mainly because of the absent deployment of real-time instruments at the remote region with harsh environments, challenging weather conditions and logistical difficulties. The real-time measurement of atmospheric aerosol chemistry with high time resolution is still relatively rare in the northern QTP until now.

Atmospheric
Chemistry
and Physics
Discussions

79   The Aerodyne aerosol mass spectrometer (AMS) is an unique instrument which can provide both
80   chemical composition and size distribution information of non-refractory submicron aerosol
81   (NR-PM$_1$) species with high time resolution and sensitivity (Jayne et al., 2000; Jimenez et al.,
82   2003; Canagaratna et al., 2007). AMS has been widely implemented worldwide in recent decades,
83   especially in China since 2006 due to the high attention to atmospheric environment (Li et al.,
84   2017, and reference therein). Besides the typical applications for studying air pollution in these
85   urban/rural sites, e.g. megacities with severe haze pollution in eastern China, AMS has also been
86   successfully deployed at many remote sites in China due to its low detection limitation (see details
87   in Table 1 of Xu et al. (2018) and Table S1 of Zhang et al. (2018)). In recent years, deployments of
88   AMS in the highland areas of QTP have been conducted in some field studies, including a
89   high-resolution time-of-flight AMS (HR-ToF-AMS) and a soot particle AMS (SP-AMS) at Nam
90   Co in the central QTP (Wang et al., 2017; Xu et al., 2018), a HR-ToF-AMS at QOMS (Zhang et al.,
91   2018) and Mt. Yulong (Zheng et al., 2017) in the southern QTP, and an Aerodyne aerosol chemical
92   speciation monitor (ACSM) at Menyuan in the northeastern QTP (Du et al., 2015). Consistent
93   with those filter samplings, the dominant contributions of organics (54−68%) but low PM$_1$
94   (NR-PM$_1$ + BC) mass loadings (2.0−5.7 μg m^{-3}) were all found in those AMS studies conducted
95   in the southern or central QTP (Zheng et al., 2017; Xu et al., 2018; Zhang et al., 2018), mainly
96   associated with the significant impacts of long-range transport biomass burning emissions from
97   southern Asia, whereas relatively few studies were conducted in the northern QTP.

98   In this study, a HR-ToF-AMS with other real-time collocated instruments were first deployed at
99   the Waliguan (WLG) Baseline Observatory, which was one of the World Meteorological
100   Organization's (WMO) Global Atmospheric Watch (GAW) baseline observatories, located in the
101   northeastern QTP, to characterize the submicron aerosol chemical compositions and sources
102   during summer season. The 5-min real-time characterizations of submicron aerosols including
103   mass concentrations, chemical composition, size distribution as well as temporal and diurnal
104   variations were presented in details in this study. Source apportionment using positive matrix
105   factorization (PMF) analysis on the high-resolution mass spectrum of organic aerosol (OA) was
106   conducted to investigate the sources and chemical evolution of OA during long-range transport.
107   Finally, back trajectories of air masses were then performed to present the possible sources and
108   pathway of ambient aerosols during the sampling period.

2 Experimental methods

2.1 Site and measurements

111   The field study was carried out during 1−31 July 2017 within the typical warm and rainy season at
112   the Waliguan (WLG) Baseline Observatory (36°17′ N, 100°54′ E, 3816 m a.s.l.), which locates in
113   the top of Mt. Waliguan at the northeastern edge of QTP in western China with an ~ 600 m
114   elevation difference from the surrounding ground (Fig. 1a and b). Mt. Waliguan is a relatively
115   remote area and generally covered by typical highland vegetation, e.g., highland grassland and
116   tundra, and constructed as an in-land baseline station of Global Atmosphere Watch (GAW) since
117   1994 (http://www.wmo.int/pages/prog/arep/gaw/gaw_home_en.html). The closest town, GongHe
118   County, is located ~ 30 km to the west of Mt. Waliguan and with a population of ~ 30,000, while

Atmospheric
Chemistry
and Physics
Discussions

119 Xining, the capital city of Qinghai Province, China, is the closest concentrated population center
120 located about 90 km to the northeast and with a population of 2.35 millions. A national road is
121 about 9 km to the north of Mt. Waliguan, yet with relative light vehicle traffic. Therefore, there are
122 no strong anthropogenic source emissions around Mt. Waliguan. The date and time used in this
123 study are reported in local time, i.e., Beijing Time (BJT: UTC + 8 h).

2.2 Instrumentation

125 Aerosol particle measurements were performed at the top floor of the main two-story building at
126 WLG observatory with a suit of real-time instruments, including a HR-ToF-AMS (Aerodyne
127 Research Inc., Billerica, MA, USA) for 5 min size-resolved chemical compositions (organics,
128 sulfate, nitrate, ammonium and chloride) of NR-PM$_1$, a photoacoustic extinctiometer (PAX, DMT
129 Inc., Boulder, CO, USA) for particle light absorption and scattering coefficients (b_{abs} and b_{scat}) at
130 405 nm and the black carbon (BC) mass concentration through a constant mass absorption
131 efficient (MAE) value of 10.18 m^2 g^{-1}, and a cloud condensation nuclei counter (CCN-100, DMT
132 Inc., Boulder, CO, USA) for the number concentration of cloud condensation nuclei (CCN) that
133 can form into cloud droplets. Simultaneously, other synchronous data were also acquired at the
134 WLG baseline observatory, including the mass concentrations of PM$_{2.5}$ and PM$_{10}$ measured by a
135 TEOM 1405-DF dichotomous ambient particulate monitor with a filter dynamics measurement
136 system (Thermo Scientific, Franklin, MA, USA) and gaseous pollutants of CO and O$_3$ measured
137 using the Thermo gas analyzers (Model 48i and 49i, respectively, Thermo Scientific, Franklin,
138 MA, USA). The setup of instruments in this study was shown in Fig. 1d. Ambient particles were
139 sampled through an inlet system, including a PM$_{2.5}$ cyclone (model URG-2000-30EH, URG Corp.,
140 Chapel Hill, NC, USA) for removing coarse particles with size cutoffs of 2.5 μm, a nafion dryer
141 following the cyclone to dry the ambient air and eliminate the potential humidity effect on
142 particles, and 0.5 inch stainless steel tubes. The inlet stepped out of the building rooftop about 1.5
143 m, and the total air flow of the inlet was about 12.5 L min^{-1}, maintained by a vacuum pump with a
144 flow rate of 10 L min^{-1} for the PM$_{2.5}$ size cut, and the other part of flow rate by the instruments.
145 The room temperature was maintained at ~ 18 °C by two air conditioners. In addition, a Vantage
146 Pro2 weather station (Davis Instruments Corp., Hayward, CA, USA) was set up on the building
147 rooftop to obtain the real-time meteorology data, including ambient temperature (T), relative
148 humidity (RH), wind speed (WS), wind direction (WD), solar radiation (SR), and precipitation
149 (Precip.).

150 The details of the Aerodyne HR-ToF-AMS has been described elsewhere (DeCarlo et al., 2006).
151 Briefly, a 120 μm critical orifice (replaced the typical 100 μm for enhancing the transmission
152 efficiency at high-altitude area) and an aerodynamic lens were settled in the front inlet system to
153 sample and focus the ambient particles into a concentrated and narrow beam. The focused particle
154 beam exiting the lens was accelerated into the particle-sizing vacuum chamber to obtain the
155 aerodynamic size of particles by a rotating wheel chopper. Then, particles were vaporized
156 thermally at ~ 600 °C by a resistively heated surface and ionized by a 70 eV electron impact, and
157 finally, detected by a high-resolution mass spectrometer. The chopper generally worked at three
158 positions alternately, i.e., open, close, and chopping positions, for measuring the bulk and
159 background signals as well as the size-resolved spectral signals of airborne particles, respectively.

160 In this study, the mass spectrometer was toggled under the high sensitive V-mode (detection limits

161 ~ 10 ng m^{-3}) and the high resolution W-mode (~ 6000 m/Δm) every 5 min. Under the V-mode

162 operation, the instrument also switched between the mass spectrum (MS) mode and the particle

163 P-ToF mode every 15 s to obtain the mass concentrations and size distributions of NR-PM$_1$

164 species, respectively, whereas the high resolution W-mode was used to obtain high resolution mass

165 spectral data.

166 **2.3 Data processing**

167 The HR-ToF-AMS data were processed using the standard AMS analysis software of SQUIRREL

168 (v1.56) to determine the mass concentrations and size distributions of NR-PM$_1$ species and the

169 high resolution data analysis software of PIKA (v1.15c) to analyze the ion-speciated mass spectra,

170 components and elemental composition (e.g., oxygen-to-carbon (O/C), hydrogen-to-carbon (H/C),

171 nitrogen-to-carbon (N/C) and organic mass-to-organic carbon (OM/OC)) of organics in this study.

172 A collection efficiency (CE) was introduced to compensate for the incomplete transmission and

173 detection of particles due to particle bouncing at the vaporizer and partial transmission through the

174 aerodynamic lens. Middlebrook et al. (2012) had evaluated the dependency of CE on several

175 ambient properties and concluded a composition-dependent CE parameterization according to the

176 sampling line RH, aerosol acidity, and mass fraction of ammonium nitrate (ANMF). High RH,

177 high aerosol acidity or high ANMF values would all increase the CE obviously. However, in this

178 study, (1) aerosol particles were dried totally through a nafion dryer in the inlet system and made

179 sure that RH in the sampling line were below 40%; (2) aerosol particles were just slightly acidic as

180 indicated by the average ratio (0.86) of measured ammonium to predicted ammonium (see Sect.

181 3.1 and Fig. 3a for details); (3) ANMF values were normally below 0.4 during the entire sampling

182 period as shown in Fig. S1. Therefore, these three parameters were all expected to have negligible

183 effects on the quantification of aerosol species from our AMS data set and thus a constant CE of 0.5,

184 which has been widely used in previous field AMS studies, was finally employed in this study. The

185 source apportionment of organics in this study was conducted by Positive matrix factorization

186 (PMF) analysis using the PMF2.exe algorithm (v4.2) (Paatero and Tapper, 1994) and PMF

187 Evaluation Tool (PET, v2.03) (Ulbrich et al., 2009) in robust mode on the high resolution organic

188 mass spectrum. Note that the data and error matrices input into the PMF analysis were generated

189 from analyzing the V-mode data via PIKA fitting rather than W-mode in this study due to the low

190 aerosol mass loading at WLG. The PMF analysis was thoroughly evaluated following the

191 procedures summarized in Table 1 of Zhang et al. (2011), including modifying the error matrix,

192 down-weighting or removing the low signal-to-noise (S/N) ions. For example, the signals of H_2O^+

193 and CO^+ for organics were scaled to that of CO_2^+ during this study as $CO^+ = CO_2^+$ and

194 $H_2O^+ = 0.225 \times CO_2^+$ according to Aiken et al. (2008), while signals of HO^+ and O^+ were set as

195 $HO^+ = 0.23 \times H_2O^+$ and $O^+ = 0.04 \times H_2O^+$ based on the fragmentation pattern of water

196 molecules (Xu et al., 2014b), respectively. Then the above four ions were further down-weighted

197 by increasing their errors by a factor of 2 in PMF analysis. Isotopic ions were generally excluded

198 because their signals are not directly measured. The "bad" ions with $S/N < 0.2$ were removed from

199 the data and error matrices, while the "weak" ions with $0.2 < S/N < 2$ were downweighted by

200 increasing their errors. In addition, some runs with huge residual spikes, e.g., data with much too

201 low mass loadings related with the heavy rain on 27 July 2017, were also removed from the data

202   and error matrices. Finally, a four-factor solution with fPeak = 0 was chosen in this study by
203   examining the model residuals and Q/Q_{exp} contributions for each m/z and time, as well as
204   comparing the mass spectra of individual factor with reference spectra and the time series of
205   individual factor with external tracers. The mass spectra, time series, and diurnal variations of
206   PMF results from three-factor and five-factor solutions were also shown in Fig. S2 and S3 for
207   comparison, respectively. The three-factor solution did not separate the two biomass burning
208   factors whereas the five-factor solution showed a splitting factor.

3 Results and discussion

3.1 Size-resolved chemical characteristics of PM$_1$

211   An overview of temporal variations of mass concentrations and fractions of PM$_1$ chemical species
212   (organics, sulfate, nitrate, ammonium, chloride and BC) as well as meteorological conditions (T,
213   RH, WS, WD, and Precip.), mass concentrations of relevant particulate matters (PM$_{2.5}$ and PM$_{10}$)
214   and gaseous pollutants (O$_3$ and CO), and mass fractions of organic components are shown in Fig.
215   2, respectively. Missing data are due to hardware or software malfunction, maintenance of the
216   instrument, or removing large spikes and unique burning event in data processing. Air temperature
217   (T) ranged from 8.5 to 14.5 °C for the averaged diurnal variation during the study, with an average
218   ($\pm 1\sigma$) of 11.0 $\pm$ 2.0 °C, while relative humidity (RH) ranged from 55.9 to 73.5% with an average
219   of 66.6 $\pm$ 5.7% (Fig. S4). The wind directions (WD) at WLG were predominantly by eastern,
220   southeastern and northeastern during this study, with an average wind speed (WS) of 4.4 $\pm$ 2.8 m
221   s^{-1} (Fig. 1c and 2b). In addition, WD generally changed from eastern to southeastern during the
222   nighttime with WS higher than 4 m s^{-1}, whereas from northwestern to northeastern during the
223   daytime with relatively lower WS (Fig. S4). Two moderate rain events occurred during 2−9 and
224   22−28 July 2017, with daily mean values of 2.6 and 7.4 mm d^{-3}, respectively (Fig. 2a).

225   The total PM$_1$ mass varied dynamically throughout this study with 5-min mass concentration
226   ranging from 0.3 to 28.1 µg m^{-3}. This dynamic variation pattern could also be found for the mass
227   concentrations of PM$_{2.5}$, PM$_{10}$ and CO, with their correlation coefficients (R^2) versus PM$_1$ varying
228   reasonably from 0.39 to 0.63 (Fig. 2 and S4). In addition, PM$_1$ accounted 66% of PM$_{2.5}$ mass in
229   this study (Fig. S5), reflecting essentially contribution of submicron aerosols at WLG. Overall,
230   average mass concentration of total PM$_1$ ($\pm 1\sigma$) at WLG for the entire study was 9.1 ($\pm$ 5.3) µg m^{-3},
231   which was much higher than those at other high-elevation sites in the QTP measured with
232   Aerodyne AMS, such as 2.0 µg m^{-3} between 31 May and 1 July 2015 at Nam Co Station (4730 m
233   a.s.l.) in the central of QTP (Xu et al., 2018), 4.4 µg m^{-3} between 12 April and 12 May 2016 at
234   QOMS (4276 m a.s.l.) at the southern edge of QTP (Zhang et al., 2018), and 5.7 µg m^{-3} between
235   22 March and 14 April 2015 at Mt. Yulong (3410 m a.s.l.) at the southeastern edge of QTP (Zheng
236   et al., 2017), whereas this value was comparable with that (11.4 µg m^{-3}) measured with an
237   Aerodyne ACSM between 5 September and 15 October 2013 at Menyuan (3295 m a.s.l.) at the
238   northeastern QTP (Du et al., 2015). The high mass concentration at WLG was likely due to the
239   relatively shorter distance from the polluted city center and strongly mountain-valley breeze
240   during summer. Sulfate and organics were the two dominant PM$_1$ species at WLG, accounting for
241   38.1% and 34.5% on average, respectively, followed by ammonium (15.2%), nitrate (8.1%), BC

Atmospheric
Chemistry
and Physics
Discussions

242 (3.0%) and chloride (1.1%). This chemical composition of PM_1 at WLG was quite different with
243 those at Nam Co, QOMS and Mt. Yulong sites in the central or southern QTP (Zheng et al., 2017;
244 Xu et al., 2018; Zhang et al., 2018), where organics was the dominant species accounting for
245 54−68% of total PM_1 mass due to the significant contribution of biomass burning emissions,
246 whereas sulfate only contributed 9−15% of total PM_1. The consistent high contribution of sulfate
247 was also observed at Menyuan (28%) in the northeastern QTP and other rural and remote sites
248 (19−64%) in East Asia which were far away from urban areas, as that summarized in Fig. 1 in Du
249 et al. (2015). Moreover, as displayed in Fig. 3b, mass contribution of sulfate increased
250 significantly with the increase of total PM_1 mass (lower than 15% for PM_1 mass equal to 1.0 µg
251 m^{-3} and increased to more than 45% for PM_1 mass of 20.0 µg m^{-3}), suggesting important
252 contribution of sulfate to submicron aerosols at WLG.

253 Bulk acidity of PM_1 at WLG was also evaluated according to the method in Zhang et al. (2007),
254 namely using the ratio of measured ammonium to the predicted ammonium that calculated based
255 on the mass concentrations of sulfate, nitrate and chloride and assumed full neutralization of these
256 anions by ammonium. The PM_1 appeared to be slightly acidic throughout this study, as indicated
257 by the scatter plot between the measured and predicted ammonium in Fig. 3a (Slope = 0.86, R^2 =
258 0.98). The acidic feature of aerosol particles at WLG was consistent with those results at Menyuan
259 (Du et al., 2015) and Qilian Shan Mountain (Xu et al., 2015) that both located in the northeastern
260 QTP, but different with those at Nam Co (Xu et al., 2018) and QOMS (Zhang et al., 2018) in the
261 central or southern edge of QTP where bulk aerosol particles were generally neutralized or
262 excesses of ammonium. The enriched sulfate in the northeastern QTP might be related tightly with
263 the enhanced coal consumption in the northwest of China and aqueous processing by cloud at the
264 mountains. This conclusion could be further demonstrated by the emission distribution of sulfur
265 dioxide (SO_2) in China observed by the OMI satellite instrument in previous studies (Lu et al.,
266 2011; van der A et al., 2017), where SO_2 showed considerable concentrations in the northwest of
267 China, especially in urban areas like Xining and Lanzhou cities, whereas extremely low
268 concentrations occurred in the southern QTP.

269 The average chemically-resolved size distributions of mass concentrations of NR-PM_1 species are
270 shown in Fig. 3c. Overall, all chemical species peaked at the accumulation mode with different
271 peaking sizes, e.g. ~ 400 nm in aerodynamic diameter (D_{va}) for organics, ~ 450 nm for chloride,
272 and ~ 500 nm for the rest three secondary inorganic species (sulfate, nitrate and ammonium),
273 indicating the well mixed and highly aged aerosol particles at WLG during the sampling period.
274 Moreover, organics presented relatively wider distribution than the three secondary inorganic
275 species in the small sizes (< 300 nm). This could also be clearly revealed by the variations of mass
276 contribution of chemical species as a function of particle sizes in Fig. 3d. The contribution of
277 organics decreased apparently with the increasing sizes whereas those of three inorganic species,
278 especially sulfate, increased correspondingly. Specifically, organics could contributed more than
279 half of the ultrafine NR-PM_1 (D_{va} < 100 nm) that maybe associated with the existing of relatively
280 fresh sources of organic particles, while the three inorganic species dominated (more than 60%) at
281 the accumulation mode due to their highly aged properties.

282 **3.2 Bulk characteristics and elemental composition of OA**

283   The average high-resolution mass spectrum (HRMS) and elemental compositions of OA during
284   the study were shown in Fig. 4a. Note that the elemental ratios of O/C, H/C, N/C and OM/OC in
285   this study were all determined using the "improved-ambient" method (Canagaratna et al., 2015),
286   which increased O/C by 29%, H/C by 14 % and OM/OC by 15% on average, respectively,
287   comparing with those determined from the "Aiken ambient" method (Aiken et al., 2008) (Fig. S6).
288   The average HRMS of OA was quite similar with those at other locations, e.g., Menyuan (Du et al.,
289   2015), Nam Co (Xu et al., 2018) and QOMS (Zhang et al., 2018) in the QTP, with significantly
290   high contribution at m/z 44 (composed by CO_2^+; 17.9%). On average, $C_xH_yO_1^+$ dominated the
291   total OA (44.0%) followed by $C_xH_y^+$ (27.9%), $C_xH_yO_2^+$ (21.7%), $H_yO_1^+$ (5.1%), $C_xH_yN_p^+$
292   (1.0%) and $C_xH_yO_zN_p^+$ (0.2%), as shown in pie chart in Fig. 4a. The total contributions of the two
293   major oxygenated ion fragments ($C_xH_yO_z^+$) was 65.7% at WLG, which was comparable to those
294   values at Nam Co during 31 May–1 July 2015 (57.9%; Xu et al., 2018) and QOMS during 12
295   April–12 May 2016 (66.2%; Zhang et al., 2018), whereas much higher than that (38.0%) measured
296   during 11 July–7 August 2012 at Lanzhou, an urban city located at the northeastern edge of QTP
297   (Xu et al., 2014b). In addition, the average O/C ratio of 0.99 in this study was also comparable
298   with those at Nam Co (0.88; determined by "improved-ambient" method and similarly hereinafter;
299   Xu et al., 2018) and QOMS (1.07; Zhang et al., 2018), but quite higher than those observed at
300   various urban and rural sites in China during summertime, e.g., 0.53 and 0.56 in Beijing, 0.40 in
301   Shanghai, 0.41 in Shenzhen and 0.36 in Jiaxing (Hu et al., 2017). As either the contributions of
302   CO_2^+ and $C_xH_yO_z^+$ or element ratio of O/C are generally considered as good indicators for the
303   aging degree of OA, the relatively higher values at WLG as well as at other sites in the QTP
304   together indicated that OA in the QTP was highly oxidized due to the absence of local emissions
305   and long-range transport.

306   Diurnal cycles of O/C and OM/OC ratios in this study varied shallowly within 0.96−1.05 and
307   2.40−2.52, respectively, suggesting an overall regional transport organic aerosol source at WLG
308   (Fig. 4b). The relatively higher values during afternoon (16:00−17:00 BJT) but lower values
309   during morning (9:00−10:00 BJT) were mainly related to the different aerosol sources and
310   photochemical oxidation conditions during long-range transport. Besides, the ratios of O/C and
311   OM/OC were relatively stable and even higher during nighttime than those in the morning, which
312   may be induced by the consistent OA source from long-range transport at night whereas relatively
313   fresh OA enhanced in the morning. Correspondingly, the H/C ratio presented an opposite diurnal
314   pattern comparing with O/C. The elemental ratios in the Van Krevelen diagram (H/C versus O/C),
315   which had been used widely to probe the oxidation reaction mechanisms for bulk OA, were
316   calculated following a slope of –0.64 in this study (Fig. S6), which suggested that the OA
317   oxidation mechanism at WLG was a combination of carboxylic acid groups with fragmentation
318   and alcohol/peroxide functional groups without fragmentation (Heald et al., 2010).

3.3 Source apportionment of OA

320   PMF analysis on the HRMS of OA identified four distinct components, i.e., a traffic-related
321   hydrocarbon-like OA (HOA), a relatively fresh biomass burning OA (BBOA), an aged biomass
322   burning OA (agBBOA) and a more-oxidized oxygenated OA (OOA) in this study. Each of OA
323   components had unique characteristics on mass spectral profile, average element ratios, diurnal

324 pattern, and temporary variation as well as tight correlations with corresponding tracers. The

325 details on the source apportionment results of OA are given as follows.

326 Figure 5 shows the average HRMS and temporal variation of each OA component, respectively. A

327 traffic-related hydrocarbon-like OA (HOA), with the lowest O/C ratio (0.33) and the highest H/C

328 ratio (1.83) among the four factors, was identified in this study. Similar to several HOA mass

329 spectra reported in previous studies, HRMS of HOA in this study was also dominated by

330 hydrocarbon ion series of $C_nH_{2n\pm1}^+$, especially $C_3H_5^+$ ($m/z = 41$), $C_3H_7^+$ ($m/z = 43$), $C_4H_7^+$ ($m/z =$

331 55), $C_4H_9^+$ ($m/z = 57$), $C_5H_9^+$ ($m/z = 69$), and $C_5H_{11}^+$ ($m/z = 71$), as shown in Fig. 5a.

332 Consequently, the dominant contribution of ion fragment was $C_xH_y^+$ (62.8%) follow by $C_xH_yO_1^+$

333 (29.3%) and $C_xH_yO_2^+$ (6.1%) (Fig. S7), suggesting the primary feature of HOA compared with

334 other OA components. The two dominant ions, m/z 57 (mainly $C_4H_9^+$ and $C_3H_5O^+$) and m/z 55

335 (mainly $C_4H_7^+$ and $C_3H_3O^+$), which are generally associated with primary organics from

336 combustion sources, are commonly considered as tracers for HOA in previous studies (Zhang et

337 al., 2005). In our study, HOA contributed 71 and 27% to $C_4H_7^+$ and $C_3H_3O^+$, respectively, at m/z

338 55 while 89 and 29% to $C_4H_9^+$ and $C_3H_5O^+$ at m/z 57. The time series of HOA correlated closely

339 with those of $C_4H_9^+$ ($R^2 = 0.68$, Fig. 5e) and other alkyl fragments, like $C_3H_7^+$, $C_4H_7^+$, $C_5H_9^+$ (R^2

340 = 0.52−0.65, Fig. S8). Besides, the mass spectrum of HOA was highly similar to those from other

341 locations around the world (Aiken et al., 2009; Elser et al., 2016; Hu et al., 2016), with correlation

342 coefficients (R^2) varying from 0.62 to 0.94 (Fig. S9). Diurnal variation of HOA (Fig. 6c and d) in

343 this study presented two slight peaks in the late morning (around 10:00 BJT) and evening (around

344 20:00 BJT), respectively. Note that the O/C ratio of HOA in this study was obviously higher than

345 those (generally lower than 0.2) observed in either urban sites or laboratory studies where have

346 intense local traffic emissions (He et al., 2010; Sun et al., 2011; Xu et al., 2016). The reason is

347 mainly due to the regional transport of traffic emission to WLG. As mentioned in Sect. 2.1, one

348 national road is about 9 km to the north of Mt. Waliguan yet with relative light vehicle traffic.

349 Hence, the traffic related aerosols from either the national road or nearby towns and cities would

350 undergo certain oxidation processes during transportation to WLG site.

351 Two biomass burning related OA factors with distinctly different oxidation degrees were also

352 found in this study. The O/C and OM/OC ratios for the relatively fresh biomass burning OA

353 (BBOA) were 0.69 and 2.06, respectively, while the aged biomass burning OA (agBBOA) showed

354 much higher elemental ratios with O/C of 1.02 and OM/OC of 2.49. Correspondingly, the

355 $C_xH_yO_z^+$ fragment also showed high contribution for agBBOA than that for BBOA (67.8% vs.

356 56.6%; Fig. S7). Although the m/z 44 (composed by CO_2^+) signals were still the highest peaks in

357 both the two factors, the m/z 60 (composed by $C_2H_4O_2^+$) signals, which were generally regarded

358 as well-known tracers for biomass burning emissions (Alfarra et al., 2007), was higher in BBOA

359 than agBBOA HRMS (0.51% vs. 0.46%). In addition, both the fractions of $C_2H_4O_2^+$ in their

360 HRMS were higher than the typical value of < 0.3% in the absence of biomass burning impacts

361 (Cubison et al., 2011). As shown in the Fig. 5, the time series of agBBOA correlated tightly with

362 $C_2H_4O_2^+$ ($R^2 = 0.79$) and sulfate ($R^2 = 0.47$), while BBOA corrected well with $C_2H_4O_2^+$ ($R^2 =$

363 0.47) and potassium ($R^2 = 0.30$), respectively. The time series of agBBOA also corrected well with

364 $C_xH_yO_1^+$ and $C_xH_yO_2^+$ ions, while BBOA corrected well with $C_xH_y^+$ and $C_xH_yO_1^+$ (Fig. S8). In

365 addition, both the mass spectra of the two biomass burning related OA factors resembled well with

Atmospheric
Chemistry
and Physics
Discussions

366   that of BBOA at QOMS (R^2 of 0.886 and 0.954, respectively; Fig. S9; Zhang et al., 2018),

367   whereas correlated slightly weaker ($R^2 = 0.39$–0.59) with other standard BBOA mass spectrums at

368   other sites around the world (Aiken et al., 2009; Mohr et al., 2012). The agBBOA mass spectrum

369   in this study correlated tightly ($R^2 = 0.914$) with the less oxidized oxygenated OA (LOOOA)

370   identified at Nam Co station (Fig. S9; Xu et al., 2018). All these comparisons and correlation

371   analysis further verified the reasonable source apportionment of OA in this study, namely there

372   were two biomass burning related OAs at WLG which had different oxidation degrees likely due

373   to their different sources and/or transport distances (see Sect. 3.4 for details). Similar OA source

374   apportionment of two BBOA components with different oxidation degrees have also been resolved

375   in previous studies, e.g., an additional oxygenated biomass-burning-influenced organic aerosol

376   (OOA$_2$-BBOA or OOA-BB) in the Paris metropolitan area (Crippa et al., 2013), urban Nanjing

377   (Zhang et al., 2015) and Mt. Yulong (Zheng et al., 2017), respectively, besides the relatively fresh

378   BBOA component. Moreover, the O/C ratio of BBOA in this study was also obviously higher than

379   those in other urban or rural sites in China where had direct or local biomass burning sources, e.g.,

380   0.24 in Lanzhou (Xu et al., 2016), 0.36 in Beijing (Sun et al., 2016) and 0.26 in Kaiping (Huang et

381   al., 2011). The diurnal patterns of the two biomass burning related OAs presented nearly opposite

382   trends in this study (Fig. 6c and d), with high values during the nighttime and decreased trend in

383   the afternoon for BBOA whereas increased obviously during the daytime for agBBOA, mainly

384   associated with the possible aging evolution from BBOA to agBBOA via photochemical oxidation

385   during the daytime.

386   Another OA component, characterized by the highest peak at m/z 44 (contributed ~ 28% of total

387   signal and composed by CO_2^+), the highest average O/C (1.42) and OM/OC (3.00), and the highest

388   contribution of $C_xH_yO_z^+$ fragment (44.5% of $C_xH_yO_1^+$ and 30.6% of $C_xH_yO_2^+$; Fig. S7) among

389   the four factors, was identified as an oxygenated OA (OOA) in this study. The OOA HRMS in this

390   study was quite similar with those more-oxidized oxygenated OA (MO-OOA) or low-volatility

391   oxygenated OA (LV-OOA) factors identified frequently in previous AMS studies, especially

392   resembled tightly to those MO-OOA identified in other QTP locations (Fig. S9), e.g. Nam Co (R^2

393   = 0.995; Xu et al., 2018) and QOMS ($R^2 = 0.997$; Zhang et al., 2018), suggesting that this factor

394   mainly represented a typical regional oxygenated OA. The time series of OOA in this study

395   correlated closely with the main secondary inorganic species, sulfate ($R^2 = 0.51$), indicating their

396   commonly regional and aged properties. In addition, the time series of OOA also corrected well

397   with $C_xH_yO_2^+$ ions, especially with CO_2^+ ($R^2 = 0.62$) as shown in Fig. S8. Although OOA

398   showed relatively stable contributions during the whole day, the diurnal variation of OOA mass

399   concentration presented low values in the late morning, continuously increasing trend during the

400   afternoon and moderate values during nighttime (Fig. 6c and d), suggesting that OOA diurnal

401   pattern was mainly driven by the combine effects of PBL variation and photochemical activities.

402   Overall, the average mass concentration of organics was 3.14 µg m^{-3} for the entire study and

403   composed by 34.4% of OOA, 40.4% of agBBOA, 18.4% of BBOA and 6.8% of HOA on average

404   (Fig. 6a). The biomass burning related OA components together contributed more than half of the

405   total organics. In addition, obviously enhanced contributions were found for the two biomass

406   burning related OA components, particular for agBBOA, with the increasing organics mass,

407   whereas OOA decreased correspondingly (Fig. 6b). For example, BBOA and agBBOA contributed

Atmospheric
Chemistry
and Physics
Discussions

408   only ~ 10% to total organics when OA was less than 1.0 µg m^{-3}, whereas the contribution reached

409   up to 70% with the mass concentration of OA increased to 7 µg m^{-3}. Moreover, the important

410   contribution of agBBOA could also be clearly seen in the temporal variations in Fig. 2f, where

411   agBBOA dominated organics during the relatively polluted periods. All of these suggested that

412   biomass burning emissions from regional transport was the important source for OA at WLG. The

413   triangle plot (f44 vs. f43 or fCO$_2^+$ vs. fC$_3$H$_3$O$^+$), which has been widely used in AMS studies, was

414   an useful method to characterize the possible evolution mechanism of organic components upon

415   aging in the ambient atmosphere (Ng et al., 2010). As shown in Fig. 4c and d, the majority of data

416   are distributed within the two dash lines that defined as the general triangular space where ambient

417   organic components fall by Ng et al. (2010). HOA presented relatively primary nature among four

418   organic components and located in the bottom of triangle plots, while two biomass related

419   components in the middle part and OOA in the upper-left corner of the triangle plots, suggesting

420   an obvious oxidation evolution from relatively primary components to secondary components.

421   **3.4 Source analysis**

422   In order to study the dominant sources and explore the influence of regional transport to PM$_1$ mass

423   loading and chemical composition at WLG during summer season, the 72 h backward air mass

424   trajectories and average clusters at 500 m above ground level were calculated at 1 h intervals using

425   the Hybrid Single Particle Lagrangian Integrated Trajectory (HYSPLIT) model (Draxler and

426   Rolph, 2003) and meteorological data from the NOAA Global Data Assimilation System (GDAS).

427   Finally, six air mass clusters were adopted in this study as presented in Fig. 7a.

428   Air masses from northeast (C1) with the shortest transport distance and lowest height among all

429   the clusters, dominated the air mass contribution (57%) and had the highest average PM$_1$ mass

430   concentration (10.8 µg m^{-3}) during the sampling period, whereas the rest five clusters (C2−C6)

431   were generally from the west or northwest and showed apparently longer transport distances,

432   higher heights and relatively lower mass concentrations (5.8−7.8 µg m^{-3}) than C1. As shown in

433   Fig. 1b, three towns (Haiyan, Huangyuan and Huangzhong) as well as the capital city (Xining) of

434   Qinghai Province were located to the northeast of WLG within 100 km, leading to relatively dense

435   population and intense industrial activities in these areas compared with those areas to the west of

436   WLG. Therefore, the prevailing air masses with low transport height for C1 could bring large

437   amount of surface anthropogenic and industrial pollutants to WLG. This conclusion could further

438   be supported by the significantly different contributions of chemical species during each cluster

439   (Fig. 7a). Specifically, C1 showed higher contribution of sulfate compared to other clusters (39.5

440   vs. 32.0−35.5%), which was mainly related with the intense industrial emissions. In addition, OA

441   components for C1 showed higher contributions from BBOA (19.5%) and agBBOA (43.3%)

442   compared with those for C4 and C5 (12.3 and 11.2% for BBOA and 35.4 and 36.7% for agBBOA,

443   respectively), whereas much lower contribution of oxidized OOA was found for C1 than those for

444   C4 and C5 (31.0 vs. 43.9 and 44.0%), suggesting the relatively fresh of OA for C1. This

445   phenomenon was more clear for the two distinct periods, P1 and P2, as shown in Fig. 7b and 8. Air

446   masses for P2 was mainly from the northeast (C1; 79.0%) and resulted higher contributions from

447   sulfate (39.9% to total PM$_1$) and the two biomass burning related OA components (BBOA and

448   agBBOA, 63.2% to total organics), however, three clusters (C4−C6) from the west with long

449 transport distances dominated P1 and led to significant enhancement of OOA contribution.

450 Besides the back trajectory analysis, bivariate polar plot analysis was another useful method to
451 give insight into the potential source regions of ambient aerosols, which presents the relationships
452 of mass concentrations of PM_1 chemical species with wind conditions (WS and WD) (Fig. S10).
453 All species showed elevated mass concentrations from east, however, with different hotspots for
454 various species, suggesting their probably distinct sources and impacts from regional transport.
455 The three main inorganic species (sulfate, nitrate and ammonium) and aged OOA generally had
456 hotspots from the northeast in accordance with the predominant air masses from northeast during
457 the daytime where showed more intensive anthropogenic and industrial emissions. Whereas
458 chloride, BC and BBOA had obvious hotspots from southeast with wind speed around 10 m s^{-1},
459 which were mainly associated with the possible burning emissions of residents located to the
460 southeast of WLG during the nighttime.

461 **4 Conclusions**

462 In this study, the highly time-resolved physicochemical properties of submicron aerosols were
463 investigated during summer 2017 at a high-altitude background station in the northeastern QTP,
464 using a suit of real-time instruments including HR-ToF-AMS, PAX, etc. The major findings
465 include the following:

466   1. The 5-min mass concentration of total PM_1 (NR-PM_1 + BC) varied dynamically between 0.3
467   and 28.1 µg m^{-3} during this study, with an average PM_1 mass loading of 9.1 (± 5.3) µg m^{-3},
468   which was higher than those measured with Aerodyne AMS at other high-elevation sites in
469   the southern or central QTP. Different with the significant impacts of biomass burning
470   emissions in the southern QTP, sulfate showed dominant contribution (38.1%) at WLG. In
471   addition, mass contribution of sulfate increased obviously with the increase of PM_1 mass
472   loading, indicating the apparently regional transport of sulfate from inland areas in
473   northwestern China. Correspondingly, PM_1 appeared to be slightly acidic throughout this
474   study related with the enhanced sulfate contribution. All chemical species of NR-PM_1 peaked
475   at the accumulation mode, suggesting the well mixed and highly aged aerosol particles at
476   WLG during the sampling period.

477   2. OA on average was dominated by 65.7% of $C_xH_yO_z^+$ ion fragment, with the average O/C
478   ratio of 0.99 and OM/OC ratio of 2.44, indicating its highly aged property at this remote site.
479   PMF analysis performed on the OA HRMS resolved four distinct OA components, including
480   HOA, BBOA, agBBOA and OOA. On average, the two relatively oxidized OAs (OOA and
481   agBBOA) contributed 34.4% and 40.4%, respectively, while the rest were 18.4% for BBOA
482   and 6.8% for HOA. In addition, obvious enhanced contributions were found for the two
483   biomass burning related OA components with the increasing OA mass, demonstrating that
484   biomass burning emissions from regional transport was the dominant OA source at WLG.

485   3. Air masses from northeast (C1) with the shortest transport distance among the six clusters
486   presented dominant contribution (57%) and the highest PM_1 mass concentration (10.8 µg
487   m^{-3}), mainly due to the enhanced contributions of sulfate and biomass burning related OA

Atmospheric
Chemistry
and Physics
Discussions

488   components from the inland areas in northwestern China. The rest clusters (C2−C6) from the
489   west or northwest with apparently larger transport distances, however, showed relatively
490   lower mass concentrations and higher OOA contributions than C1. These source analysis
491   together suggested the distinct aerosol sources and significant impacts of regional transport
492   to aerosol mass loadings and chemical compositions at WLG during summer season.

493   *Data availability.* The processed AMS data and meteorological data in this study are available
494   upon request from the corresponding author.

495   *Author contribution.* XHZ analyzed the data and wrote the manuscript. JZX organized the
496   campaign, analyzed data, and wrote the manuscript. SCK and QZ wrote the manuscript.

References

504   Aiken, A. C., DeCarlo, P. F., Kroll, J. H., Worsnop, D. R., Huffman, J. A., Docherty, K. S., Ulbrich, I. M., Mohr, C., Kimmel, J.
505   R., Sueper, D., Sun, Y., Zhang, Q., Trimborn, A., Northway, M., Ziemann, P. J., Canagaratna, M. R., Onasch, T. B., Alfarra, M.
506   R., Prevot, A. S. H., Dommen, J., Duplissy, J., Metzger, A., Baltensperger, U., and Jimenez, J. L.: O/C and OM/OC ratios of
507   primary, secondary, and ambient organic aerosols with high-resolution time-of-flight aerosol mass spectrometry, Environ. Sci.
508   Technol., 42, 4478-4485, doi:10.1021/es703009q, 2008.
509   Aiken, A. C., Salcedo, D., Cubison, M. J., Huffman, J. A., DeCarlo, P. F., Ulbrich, I. M., Docherty, K. S., Sueper, D., Kimmel, J.
510   R., Worsnop, D. R., Trimborn, A., Northway, M., Stone, E. A., Schauer, J. J., Volkamer, R. M., Fortner, E., de Foy, B., Wang, J.,
511   Laskin, A., Shutthanandan, V., Zheng, J., Zhang, R., Gaffney, J., Marley, N. A., Paredes-Miranda, G., Arnott, W. P., Molina, L.
512   T., Sosa, G., and Jimenez, J. L.: Mexico City aerosol analysis during MILAGRO using high resolution aerosol mass
513   spectrometry at the urban supersite (T0)–Part 1: Fine particle composition and organic source apportionment, Atmos. Chem.
514   Phys., 9, 6633-6653, doi:10.5194/acp-9-6633-2009, 2009.
515   Alfarra, M. R., Prevot, A. S. H., Szidat, S., Sandradewi, J., Weimer, S., Lanz, V. A., Schreiber, D., Mohr, M., and Baltensperger,
516   U.: Identification of the Mass Spectral Signature of Organic Aerosols from Wood Burning Emissions, Environ. Sci. Technol.,
517   41, 5770-5777, doi:10.1021/es062289b, 2007.
518   Canagaratna, M. R., Jayne, J. T., Jimenez, J. L., Allan, J. D., Alfarra, M. R., Zhang, Q., Onasch, T. B., Drewnick, F., Coe, H.,
519   Middlebrook, A., Delia, A., Williams, L. R., Trimborn, A. M., Northway, M. J., DeCarlo, P. F., Kolb, C. E., Davidovits, P., and
520   Worsnop, D. R.: Chemical and microphysical characterization of ambient aerosols with the aerodyne aerosol mass
521   spectrometer, Mass Spectrom. Rev., 26, 185-222, doi:10.1002/mas.20115, 2007.
522   Canagaratna, M. R., Jimenez, J. L., Kroll, J. H., Chen, Q., Kessler, S. H., Massoli, P., Hildebrandt Ruiz, L., Fortner, E., Williams,
523   L. R., Wilson, K. R., Surratt, J. D., Donahue, N. M., Jayne, J. T., and Worsnop, D. R.: Elemental ratio measurements of organic
524   compounds using aerosol mass spectrometry: characterization, improved calibration, and implications, Atmos. Chem. Phys.,
525   15, 253-272, doi:10.5194/acp-15-253-2015, 2015.
526   Crippa, M., DeCarlo, P. F., Slowik, J. G., Mohr, C., Heringa, M. F., Chirico, R., Poulain, L., Freutel, F., Sciare, J., Cozic, J., Di
527   Marco, C. F., Elsasser, M., Nicolas, J. B., Marchand, N., Abidi, E., Wiedensohler, A., Drewnick, F., Schneider, J., Borrmann, S.,
528   Nemitz, E., Zimmermann, R., Jaffrezo, J. L., Prévôt, A. S. H., and Baltensperger, U.: Wintertime aerosol chemical composition
529   and source apportionment of the organic fraction in the metropolitan area of Paris, Atmos. Chem. Phys., 13, 961-981,
530   doi:10.5194/acp-13-961-2013, 2013.
531   Cubison, M. J., Ortega, A. M., Hayes, P. L., Farmer, D. K., Day, D., Lechner, M. J., Brune, W. H., Apel, E., Diskin, G. S., Fisher,
532   J. A., Fuelberg, H. E., Hecobian, A., Knapp, D. J., Mikoviny, T., Riemer, D., Sachse, G. W., Sessions, W., Weber, R. J.,
533   Weinheimer, A. J., Wisthaler, A., and Jimenez, J. L.: Effects of aging on organic aerosol from open biomass burning smoke in
534   aircraft and laboratory studies, Atmos. Chem. Phys., 11, 12049-12064, doi:10.5194/acp-11-12049-2011, 2011.
535   DeCarlo, P. F., Kimmel, J. R., Trimborn, A., Northway, M. J., Jayne, J. T., Aiken, A. C., Gonin, M., Fuhrer, K., Horvath, T.,
536   Docherty, K. S., Worsnop, D. R., and Jimenez, J. L.: Field-Deployable, High-Resolution, Time-of-Flight Aerosol Mass
537   Spectrometer, Anal. Chem., 78, 8281-8289, doi:10.1021/ac061249n, 2006.
538   Draxler, R. R., and Rolph, G. D.: HYSPLIT (HYbrid Single-Particle Lagrangian Integrated Trajectory) model access via NOAA
539   ARL READY website (http://www.arl.noaa.gov/ready/hysplit4.html). NOAA Air Resources Laboratory, Silver Spring, MD,
540   USA, 2003.
541   Du, W., Sun, Y. L., Xu, Y. S., Jiang, Q., Wang, Q. Q., Yang, W., Wang, F., Bai, Z. P., Zhao, X. D., and Yang, Y. C.: Chemical
542   characterization of submicron aerosol and particle growth events at a national background site (3295 m a.s.l.) on the Tibetan
543   Plateau, Atmos. Chem. Phys., 15, 10811-10824, doi:10.5194/acp-15-10811-2015, 2015.

544 Elser, M., Huang, R.-J., Wolf, R., Slowik, J. G., Wang, Q., Canonaco, F., Li, G., Bozzetti, C., Daellenbach, K. R., Huang, Y.,
545 Zhang, R., Li, Z., Cao, J., Baltensperger, U., El-Haddad, I., and Prévôt, A. S. H.: New insights into PM$_{2.5}$
546 chemical composition and sources in two major cities in China during extreme haze events using aerosol mass spectrometry,
547 Atmos. Chem. Phys., 16, 3207-3225, doi:10.5194/acp-16-3207-2016, 2016.
548 Engling, G., Zhang, Y. N., Chan, C. Y., Sang, X. F., Lin, M., Ho, K. F., Li, Y. S., Lin, C. Y., and Lee, J. J.: Characterization and
549 sources of aerosol particles over the southeastern Tibetan Plateau during the Southeast Asia biomass-burning season, Tellus B,
550 63, 117-128, doi:10.1111/j.1600-0889.2010.00512.x, 2011.
551 He, L. Y., Lin, Y., Huang, X. F., Guo, S., Xue, L., Su, Q., Hu, M., Luan, S. J., and Zhang, Y. H.: Characterization of
552 high-resolution aerosol mass spectra of primary organic aerosol emissions from Chinese cooking and biomass burning, Atmos.
553 Chem. Phys., 10, 11535-11543, doi:10.5194/acp-10-11535-2010, 2010.
554 Heald, C. L., Kroll, J. H., Jimenez, J. L., Docherty, K. S., DeCarlo, P. F., Aiken, A. C., Chen, Q., Martin, S. T., Farmer, D. K., and
555 Artaxo, P.: A simplified description of the evolution of organic aerosol composition in the atmosphere, Geophys. Res. Lett., 37,
556 L08803, doi:10.1029/2010gl042737, 2010.
557 Hu, W., Hu, M., Hu, W.-W., Zheng, J., Chen, C., Wu, Y., and Guo, S.: Seasonal variations in high time-resolved chemical
558 compositions, sources, and evolution of atmospheric submicron aerosols in the megacity Beijing, Atmos. Chem. Phys., 17,
559 9979-10000, doi:10.5194/acp-17-9979-2017, 2017.
560 Hu, W. W., Hu, M., Hu, W., Jimenez, J. L., Yuan, B., Chen, W., Wang, M., Wu, Y., Chen, C., Wang, Z., Peng, J., Zeng, L., and
561 Shao, M.: Chemical composition, sources, and aging process of submicron aerosols in Beijing: Contrast between summer and
562 winter, J. Geophys. Res. Atmos., 121, 1955-1977, doi:10.1002/2015jd024020, 2016.
563 Huang, X. F., He, L. Y., Hu, M., Canagaratna, M. R., Kroll, J. H., Ng, N. L., Zhang, Y. H., Lin, Y., Xue, L., Sun, T. L., Liu, X. G.,
564 Shao, M., Jayne, J. T., and Worsnop, D. R.: Characterization of submicron aerosols at a rural site in Pearl River Delta of China
565 using an Aerodyne High-Resolution Aerosol Mass Spectrometer, Atmos. Chem. Phys., 11, 1865-1877,
566 doi:10.5194/acp-11-1865-2011, 2011.
567 Jayne, J. T., Leard, D. C., Zhang, X. F., Davidovits, P., Smith, K. A., Kolb, C. E., and Worsnop, D. R.: Development of an aerosol
568 mass spectrometer for size and composition analysis of submicron particles, Aerosol Sci. Technol., 33, 49-70,
569 doi:10.1080/027868200410840, 2000.
570 Jimenez, J. L., Jayne, J. T., Shi, Q., Kolb, C. E., Worsnop, D. R., Yourshaw, I., Seinfeld, J. H., Flagan, R. C., Zhang, X., Smith, K.
571 A., Morris, J. W., and Davidovits, P.: Ambient aerosol sampling using the Aerodyne Aerosol Mass Spectrometer, J. Geophys.
572 Res., 108, 8425, doi:10.1029/2001jd001213, 2003.
573 Kang, S., Xu, Y., You, Q., Flügel, W.-A., Pepin, N., and Yao, T.: Review of climate and cryospheric change in the Tibetan Plateau,
574 Environ. Res. Lett., 5, 015101, doi:10.1088/1748-9326/5/1/015101, 2010.
575 Li, C., Bosch, C., Kang, S., Andersson, A., Chen, P., Zhang, Q., Cong, Z., Chen, B., Qin, D., and Gustafsson, O.: Sources of
576 black carbon to the Himalayan-Tibetan Plateau glaciers, Nat. Commun., 7, 12574, doi:10.1038/ncomms12574, 2016.
577 Li, J., Wang, G., Wang, X., Cao, J., Sun, T., Cheng, C., Meng, J., Hu, T., and Liu, S.: Abundance, composition and source of
578 atmospheric PM2.5 at a remote site in the Tibetan Plateau, China, Tellus B: Chemical and Physical Meteorology, 65, 20281,
579 doi:10.3402/tellusb.v65i0.20281, 2013.
580 Li, Y. J., Sun, Y., Zhang, Q., Li, X., Li, M., Zhou, Z., and Chan, C. K.: Real-time chemical characterization of atmospheric
581 particulate matter in China: A review, Atmos. Environ., 158, 270-304, doi:10.1016/j.atmosenv.2017.02.027, 2017.
582 Lu, Z., Zhang, Q., and Streets, D. G.: Sulfur dioxide and primary carbonaceous aerosol emissions in China and India, 1996–2010,
583 Atmos. Chem. Phys., 11, 9839-9864, doi:10.5194/acp-11-9839-2011, 2011.
584 Lüthi, Z. L., Škerlak, B., Kim, S. W., Lauer, A., Mues, A., Rupakheti, M., and Kang, S.: Atmospheric brown clouds reach the
585 Tibetan Plateau by crossing the Himalayas, Atmos. Chem. Phys., 15, 6007-6021, doi:10.5194/acp-15-6007-2015, 2015.
586 Middlebrook, A. M., Bahreini, R., Jimenez, J. L., and Canagaratna, M. R.: Evaluation of Composition-Dependent Collection
587 Efficiencies for the Aerodyne Aerosol Mass Spectrometer using Field Data, Aerosol Sci. Technol., 46, 258-271,
588 doi:10.1080/02786826.2011.620041, 2012.
589 Mohr, C., DeCarlo, P. F., Heringa, M. F., Chirico, R., Slowik, J. G., Richter, R., Reche, C., Alastuey, A., Querol, X., Seco, R.,
590 Peñuelas, J., Jiménez, J. L., Crippa, M., Zimmermann, R., Baltensperger, U., and Prévôt, A. S. H.: Identification and
591 quantification of organic aerosol from cooking and other sources in Barcelona using aerosol mass spectrometer data, Atmos.
592 Chem. Phys., 12, 1649-1665, doi:10.5194/acp-12-1649-2012, 2012.
593 Ng, N. L., Canagaratna, M. R., Zhang, Q., Jimenez, J. L., Tian, J., Ulbrich, I. M., Kroll, J. H., Docherty, K. S., Chhabra, P. S.,
594 Bahreini, R., Murphy, S. M., Seinfeld, J. H., Hildebrandt, L., Donahue, N. M., DeCarlo, P. F., Lanz, V. A., Prévôt, A. S. H.,
595 Dinar, E., Rudich, Y., and Worsnop, D. R.: Organic aerosol components observed in Northern Hemispheric datasets from
596 Aerosol Mass Spectrometry, Atmos. Chem. Phys., 10, 4625-4641, doi:10.5194/acp-10-4625-2010, 2010.
597 Paatero, P., and Tapper, U.: Positive matrix factorization: A non-negative factor model with optimal utilization of error estimates
598 of data values, Environmetrics, 5, 111-126, doi:10.1002/env.3170050203, 1994.
599 Qian, Y., Flanner, M. G., Leung, L. R., and Wang, W.: Sensitivity studies on the impacts of Tibetan Plateau snowpack pollution
600 on the Asian hydrological cycle and monsoon climate, Atmos. Chem. Phys., 11, 1929-1948, doi:10.5194/acp-11-1929-2011,
601 2011.
602 Sun, Y. L., Zhang, Q., Schwab, J. J., Demerjian, K. L., Chen, W. N., Bae, M. S., Hung, H. M., Hogrefe, O., Frank, B., Rattigan, O.
603 V., and Lin, Y. C.: Characterization of the sources and processes of organic and inorganic aerosols in New York city with a
604 high-resolution time-of-flight aerosol mass apectrometer, Atmos. Chem. Phys., 11, 1581-1602, doi:10.5194/acp-11-1581-2011,
605 2011.
606 Sun, Y. L., Du, W., Fu, P., Wang, Q., Li, J., Ge, X., Zhang, Q., Zhu, C., Ren, L., Xu, W., Zhao, J., Han, T., Worsnop, D. R., and
607 Wang, Z.: Primary and secondary aerosols in Beijing in winter: sources, variations and processes, Atmos. Chem. Phys., 16,
608 8309-8329, doi:10.5194/acp-16-8309-2016, 2016.
609 Ulbrich, I. M., Canagaratna, M. R., Zhang, Q., Worsnop, D. R., and Jimenez, J. L.: Interpretation of organic components from
610 Positive Matrix Factorization of aerosol mass spectrometric data, Atmos. Chem. Phys., 9, 2891-2918,
611 doi:10.5194/acp-9-2891-2009, 2009.
612 van der A, R. J., Mijling, B., Ding, J., Koukouli, M. E., Liu, F., Li, Q., Mao, H., and Theys, N.: Cleaning up the air: effectiveness
613 of air quality policy for SO$_2$ and NO$_x$ emissions in China,
614 Atmos. Chem. Phys., 17, 1775-1789, doi:10.5194/acp-17-1775-2017, 2017.
615 Wang, J., Zhang, Q., Chen, M., Collier, S., Zhou, S., Ge, X., Xu, J., Shi, J., Xie, C., Hu, J., Ge, S., Sun, Y., and Coe, H.: First
616 Chemical Characterization of Refractory Black Carbon Aerosols and Associated Coatings over the Tibetan Plateau (4730 m
617 a.s.l), Environ. Sci. Technol., 51, 14072-14082, doi:10.1021/acs.est.7b03973, 2017.
618 Xia, X., Zong, X., Cong, Z., Chen, H., Kang, S., and Wang, P.: Baseline continental aerosol over the central Tibetan plateau and a

Atmospheric
Chemistry
and Physics
Discussions

619   case study of aerosol transport from South Asia, Atmos. Environ., 45, 7370-7378, doi:10.1016/j.atmosenv.2011.07.067, 2011.

620 Xu, B., Cao, J., Hansen, J., Yao, T., Joswia, D. R., Wang, N., Wu, G., Wang, M., Zhao, H., Yang, W., Liu, X., and He, J.: Black
621   soot and the survival of Tibetan glaciers, Proc. Natl. Acad. Sci. USA, 106, 22114-22118, doi:10.1073/pnas.0910444106, 2009.

622 Xu, J., Wang, Z., Yu, G., Sun, W., Qin, X., Ren, J., and Qin, D.: Seasonal and diurnal variations in aerosol concentrations at a
623   high-altitude site on the northern boundary of Qinghai-Xizang Plateau, Atmos. Res., 120-121, 240-248,
624   doi:10.1016/j.atmosres.2012.08.022, 2013.

625 Xu, J., Wang, Z., Yu, G., Qin, X., Ren, J., and Qin, D.: Characteristics of water soluble ionic species in fine particles from a high
626   altitude site on the northern boundary of Tibetan Plateau: Mixture of mineral dust and anthropogenic aerosol, Atmos. Res., 143,
627   43-56, doi:http://dx.doi.org/10.1016/j.atmosres.2014.01.018, 2014a.

628 Xu, J., Zhang, Q., Chen, M., Ge, X., Ren, J., and Qin, D.: Chemical composition, sources, and processes of urban aerosols during
629   summertime in northwest China: insights from high-resolution aerosol mass spectrometry, Atmos. Chem. Phys., 14,
630   12593-12611, doi:10.5194/acp-14-12593-2014, 2014b.

631 Xu, J., Zhang, Q., Wang, Z. B., Yu, G. M., Ge, X. L., and Qin, X.: Chemical composition and size distribution of summertime
632     $PM_{2.5}$ at a high altitude remote location in the northeast of the Qinghai–Xizang (Tibet) Plateau: insights into aerosol sources
633   and processing in free troposphere, Atmos. Chem. Phys., 15, 5069-5081, doi:10.5194/acp-15-5069-2015, 2015.

634 Xu, J., Shi, J., Zhang, Q., Ge, X., Canonaco, F., Prévôt, A. S. H., Vonwiller, M., Szidat, S., Ge, J., Ma, J., An, Y., Kang, S., and
635   Qin, D.: Wintertime organic and inorganic aerosols in Lanzhou, China: sources, processes, and comparison with the results
636   during summer, Atmos. Chem. Phys., 16, 14937-14957, doi:10.5194/acp-16-14937-2016, 2016.

637 Xu, J., Zhang, Q., Shi, J., Ge, X., Xie, C., Wang, J., Kang, S., Zhang, R., and Wang, Y.: Chemical characteristics of submicron
638   particles at the central Tibetan Plateau: insights from aerosol mass spectrometry, Atmos. Chem. Phys., 18, 427-443,
639   doi:10.5194/acp-18-427-2018, 2018.

640 Xue, L. K., Wang, T., Guo, H., Blake, D. R., Tang, J., Zhang, X. C., Saunders, S. M., and Wang, W. X.: Sources and
641   photochemistry of volatile organic compounds in the remote atmosphere of western China: results from the Mt. Waliguan
642   Observatory, Atmos. Chem. Phys., 13, 8551-8567, doi:10.5194/acp-13-8551-2013, 2013.

643 Yang, K., Wu, H., Qin, J., Lin, C., Tang, W., and Chen, Y.: Recent climate changes over the Tibetan Plateau and their impacts on
644   energy and water cycle: A review, Global and Planetary Change, 112, 79-91, doi:10.1016/j.gloplacha.2013.12.001, 2014.

645 Yao, T., Thompson, L., Mosbrugger, V., Zhang, F., Ma, Y., Luo, T., Xu, B., Yang, X., Joswiak, D. R., Wang, W., Joswiak, M. E.,
646   Devkota, L. P., Tayal, S., Jilani, R., and Fayziev, R.: Third Pole Environment (TPE), Environmental Development, 3, 52-64,
647   doi:10.1016/j.envdev.2012.04.002, 2012.

648 Zhang, N., Cao, J., Liu, S., Zhao, Z., Xu, H., and Xiao, S.: Chemical composition and sources of PM2.5 and TSP collected at
649   Qinghai Lake during summertime, Atmos. Res., 138, 213-222, doi:10.1016/j.atmosres.2013.11.016, 2014.

650 Zhang, Q., Canagaratna, M. R., Jayne, J. T., Worsnop, D. R., and Jimenez, J. L.: Time- and size-resolved chemical composition
651   of submicron particles in Pittsburgh: Implications for aerosol sources and processes, J. Geophys. Res., 110, D07S09,
652   doi:10.1029/2004jd004649, 2005.

653 Zhang, Q., Jimenez, J. L., Worsnop, D. R., and Canagaratna, M.: A case study of urban particle acidity and its influence on
654   secondary organic aerosol, Environ. Sci. Technol., 41, 3213-3219, doi:10.1021/es061812j, 2007.

655 Zhang, Q., Jimenez, J. L., Canagaratna, M. R., Ulbrich, I. M., Ng, N. L., Worsnop, D. R., and Sun, Y.: Understanding
656   atmospheric organic aerosols via factor analysis of aerosol mass spectrometry: a review, Anal. Bioanal. Chem., 401,
657   3045-3067, doi:10.1007/s00216-011-5355-y, 2011.

658 Zhang, R., Wang, Y., He, Q., Chen, L., Zhang, Y., Qu, H., Smeltzer, C., Li, J., Alvarado, L. M. A., Vrekoussis, M., Richter, A.,
659   Wittrock, F., and Burrows, J. P.: Enhanced trans-Himalaya pollution transport to the Tibetan Plateau by cut-off low systems,
660   Atmos. Chem. Phys., 17, 3083-3095, doi:10.5194/acp-17-3083-2017, 2017.

661 Zhang, X., Xu, J., Kang, S., Liu, Y., and Zhang, Q.: Chemical characterization of long-range transport biomass burning emissions
662   to the Himalayas: insights from high-resolution aerosol mass spectrometry, Atmos. Chem. Phys., 18, 4617-4638,
663   doi:10.5194/acp-18-4617-2018, 2018.

664 Zhang, Y. J., Tang, L. L., Wang, Z., Yu, H. X., Sun, Y. L., Liu, D., Qin, W., Canonaco, F., Prévôt, A. S. H., Zhang, H. L., and
665   Zhou, H. C.: Insights into characteristics, sources, and evolution of submicron aerosols during harvest seasons in the Yangtze
666   River delta region, China, Atmos. Chem. Phys., 15, 1331-1349, doi:10.5194/acp-15-1331-2015, 2015.

667 Zheng, J., Hu, M., Du, Z., Shang, D., Gong, Z., Qin, Y., Fang, J., Gu, F., Li, M., Peng, J., Li, J., Zhang, Y., Huang, X., He, L., Wu,
668   Y., and Guo, S.: Influence of biomass burning from South Asia at a high-altitude mountain receptor site in China, Atmos.
669   Chem. Phys., 17, 6853-6864, doi:10.5194/acp-17-6853-2017, 2017.
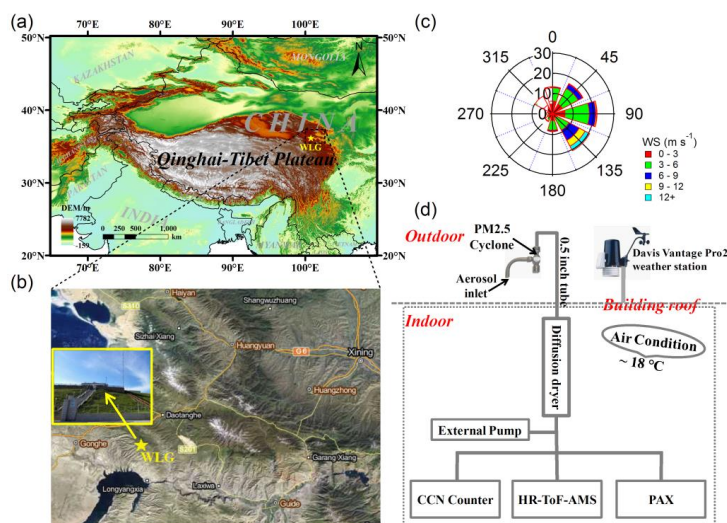
Figure 1. (a) Topography map of the Qinghai-Tibet Plateau (QTP), **(b)** location map of Mt. Waliguan Base (WLG; 36.283° N, 100.900° E, 3816 m), **(c)** the wind rose plot colored by wind speed during the field study period, and **(d)** the setup of instruments in this study.
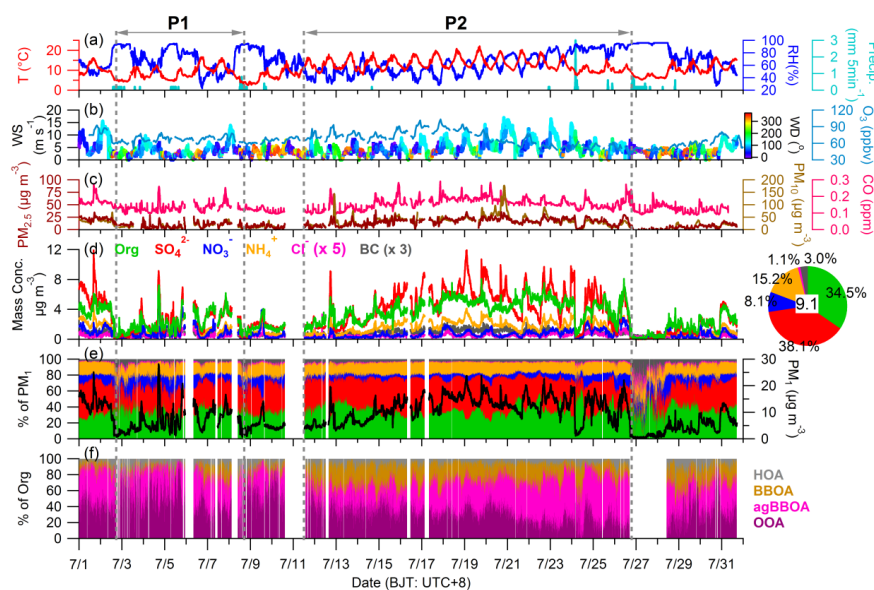

Figure 2. Time series of **(a)** ambient temperature (T), relative humidity (RH), and precipitation (Precip.), **(b)** wind speed (WS) colored by wind direction (WD) and O_3, **(c)** mass concentrations of $PM_{2.5}$, PM_{10}, and CO, **(d)** mass concentrations of PM_1 species, **(e)** mass contributions of PM_1 species as well as the total PM_1 mass concentrations, **(f)** mass contributions of four organic components. The pie chart shows the average chemical composition of PM_1 for the entire study period, with the average PM_1 mass concentration (unit of µg m^{-3}) marked in the central.
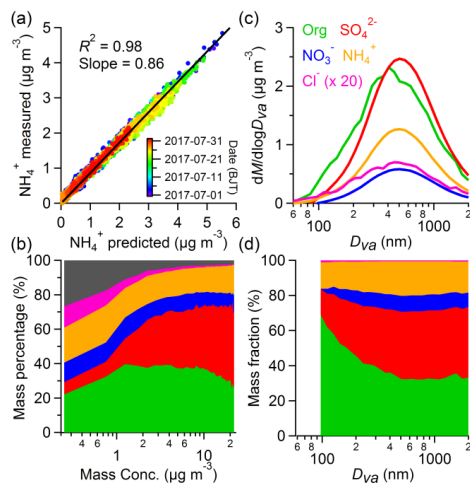
Figure 3. (a) Scatterplot and linear regression (black solid line) of measured NH_4^+ versus predicted NH_4^+ based on the mass concentrations of SO_4^{2-}, NO_3^-, and Cl^-, **(b)** the mass contributions of PM_1 chemical species as a function of total PM_1 mass concentration, and the average size distributions of **(c)** mass concentrations and **(d)** mass contributions of NR-PM_1 species in this study.
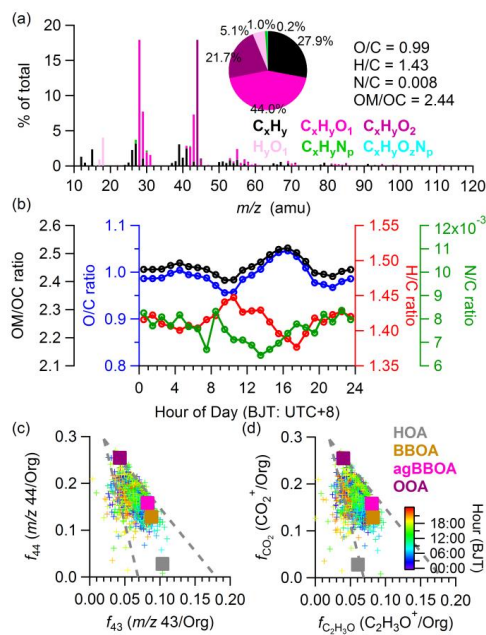

Figure 4. (a) The average high-resolution mass spectrum of organics colored with six ion categories (pie charts shows the average contributions of the six ion categories), **(b)** diurnal variations of element ratios (O/C, H/C, N/C, and OM/OC), and scatterplots of **(c)** $f44$ vs. $f43$ and **(d)** fCO_2^+ vs. $fC_2H_3O^+$ colored by time of the day, where the corresponding values of four organic components are also shown.

Atmospheric
Chemistry
and Physics
Discussions
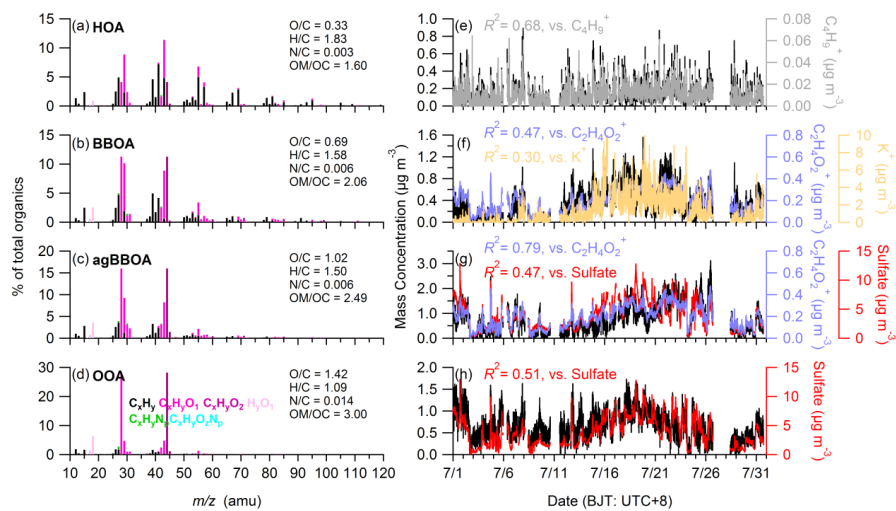

Figure 5. PMF results of (**left**) high-resolution mass spectra colored by six ion categories for the four OA factors at $m/z < 120$, (**right**) temporal variations of the four OA factors and corresponding comparison with tracer species.
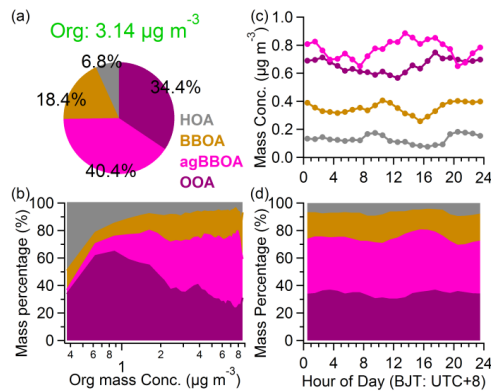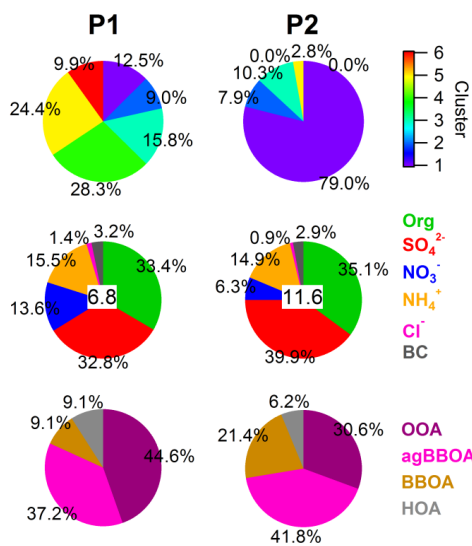

Figure 6. The average mass contributions of four organic components to total organics (**a**) during the entire study period and (**b**) as a function of total organics mass concentrations, as well as the diurnal variations of (**c**) mass concentrations and (**d**) mass contributions of four organic components in this study.
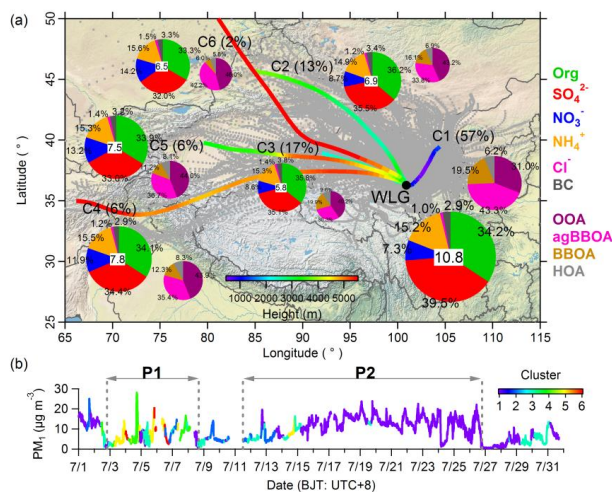
18

Figure 7. (a) The 72h backward air mass trajectories (grey dotted lines) and average trajectory clusters (solid lines colored according to height) calculated at 1 h intervals for the entire study period. Pie charts show the average mass contributions of PM$_1$ species to total PM$_1$ (average PM$_1$ mass are marked in the central of pie charts) and OA components to total organics belong to each cluster (areas of pie charts are scaled by the corresponding average mass), respectively. **(b)** Temporal variation of PM$_1$ mass concentration colored by the corresponding cluster name in this study. The markers of P1 and P2 represent two different periods that selected in this study.

Figure 8. (a) The occurrence frequency of six air mass trajectory clusters, **(b)** average contributions of PM$_1$ chemical species to total PM$_1$, and **(c)** average contributions of four organic components to total organics during P1 and P2, respectively.